A novel design approach for estimation of extreme responses of a subsea shuttle tanker hovering in ocean current considering aft thruster failure

Yihan Xing[1], Oleg Gaidai[2,*], Yucong Ma[1], Arvid Naess[3], Fang Wang[2]

[1]Department of Mechanical and Structural Engineering and Material Science, University of Stavanger, Norway

[2]Shanghai Engineering Research Centre of Marine Renewable Energy, College of Engineering Science and Technology, Shanghai Ocean University, Shanghai, China

[3]Department of Mathematical Sciences, Norwegian University of Science and Technology, Trondheim, Norway

[*]Corresponding author: gaidai@shou.edu.cn

Abstract

The subsea shuttle tanker (SST) is an innovative 33 600-ton underwater cargo tanker designed to transport CO_2 to marginal fields. These marginal fields usually have too small CO_2 volumes to justify using offshore pipelines and tanker ships. The SST travels underwater at a fixed water depth of 70 m to carry CO_2 from a land facility to a subsea well for direct injection. During offloading, the SST will approach and hover in the vicinity of the subsea well. A remotely operated vehicle (ROV) will carry and connect a flexible flowline from the subsea well to the SST. CO_2 is then offloaded via this flexible flowline. The offloading process takes four hours. During this time, the SST is subjected to time-varying current load effects, and it will dynamically keep its position using its ballast tanks, propeller, and thrusters. Knowing the extreme positional responses is essential. The extreme heave motion determines the maximum depth and correspondingly the maximum hydrostatic loading. Hydrostatic loading is a dominating load and drives the collapse design of the SST hull. Further, the extreme surge motion determines the flowline length required to avoid snap loads. In this paper, the extreme positional responses of the SST when the aft thruster fails during offloading is investigated for mean current velocities of 0.5, 1.0, and 1.5 m/s using the average conditional exceedance rate (ACER) method. The empirical data is generated using time-domain simulations with a 2D planar Simulink model.

The proposed methodology provides an accurate bivariate extreme value prediction, utilizing all available data efficiently. In this study the estimated vessel response is expressed as 5 years return level values and contours, obtained by the ACER 1D and 2D methods. Based on the overall performance of the proposed method, it was concluded that the ACER 1D and 2D methods can provide robust and accurate both univariate and bivariate predictions based on accurate numerical simulations of the vessel motion dynamics.

Keywords: Subsea technology, Submarine, LQR, ACER method, Extreme responses, Bivariate probability distribution.

1. Introduction

The subsea shuttle tanker (SST), as illustrated in Figure 1, is a novel sizeable autonomous cargo submarine first proposed by Equinor in two research disclosures in 2019 [1] and 2020 [2]. After that, Xing et al. [3] discussed the most critical design considerations surrounding the SST. Xing et al. [3] argued that for the SST to be economically attractive, it must have at least 50 % of its displacement allocated to the payload. To achieve this, Xing et al. [3] proposed using a series of design features and optimisation to reduce weight significantly in the structures, machinery, and permanent ballast. A baseline design was developed by Ma et al. [4] based on the design considerations. The baseline SST [4] is a 34 000-ton vessel designed to serve ongoing carbon capture and storage (CCS) projects in the Norwegian Continental Shelf, namely Sleipner, Utgard, and Snøhvit [5] as illustrated in Figure 2. The SST will collect CO_2 from onshore facilities off the coast of Norway and then travel autonomously subsea at a constant depth of 70 m to the subsea well for direct injection. Therefore, the SST can operate in any weather condition since it travels underwater away from wind and wave loads. The objective of the SST is to be an alternative transportation method to serve remote marginal fields where the CO_2 volumes might not be economically attractive to deploy offshore pipelines and ship tankers. In recent economic studies performed by Xing et al. [6], the SST has been proven cheaper than offshore pipelines and tanker ships for small CO_2 fields. However, the SSTs considered in Xing et al. [6] were designed using the state-of-art submarine design code DNVGL-RU-NAVAL-Pt4Ch1 [7]. The SST is expected to be even more economically attractive when design optimisations such as Jamissen et al. [8] are applied. The main design parameters of the baseline SST [4] are presented in Table 1. The baseline SST is used as the object of study in this paper.

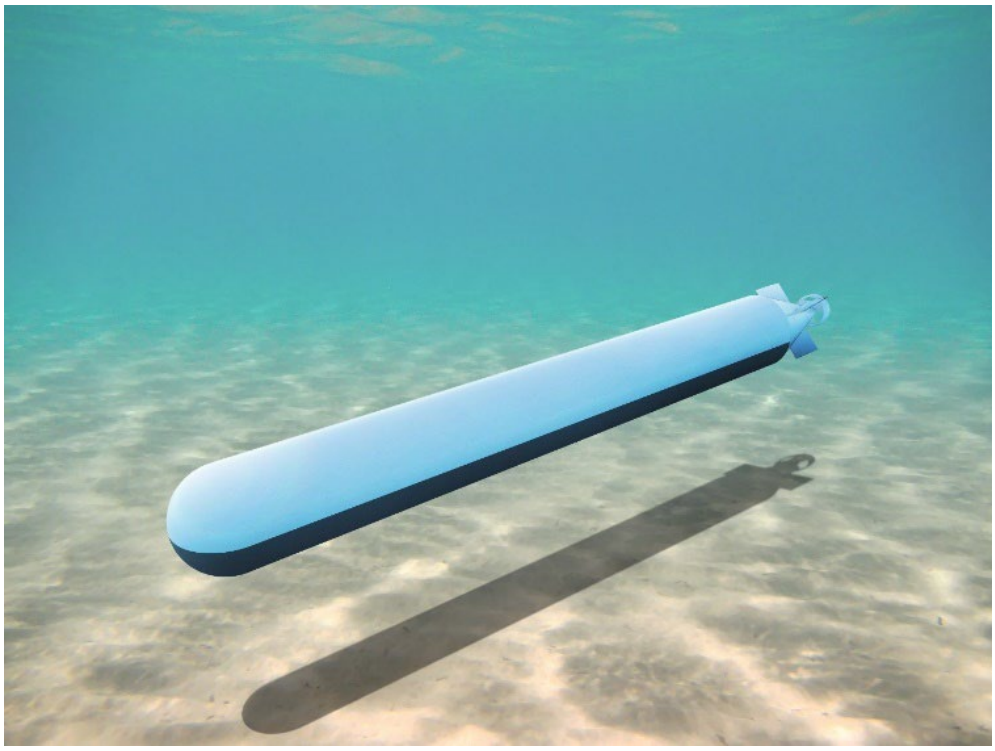

Figure 1 The Subsea Shuttle Tanker (SST) [4].

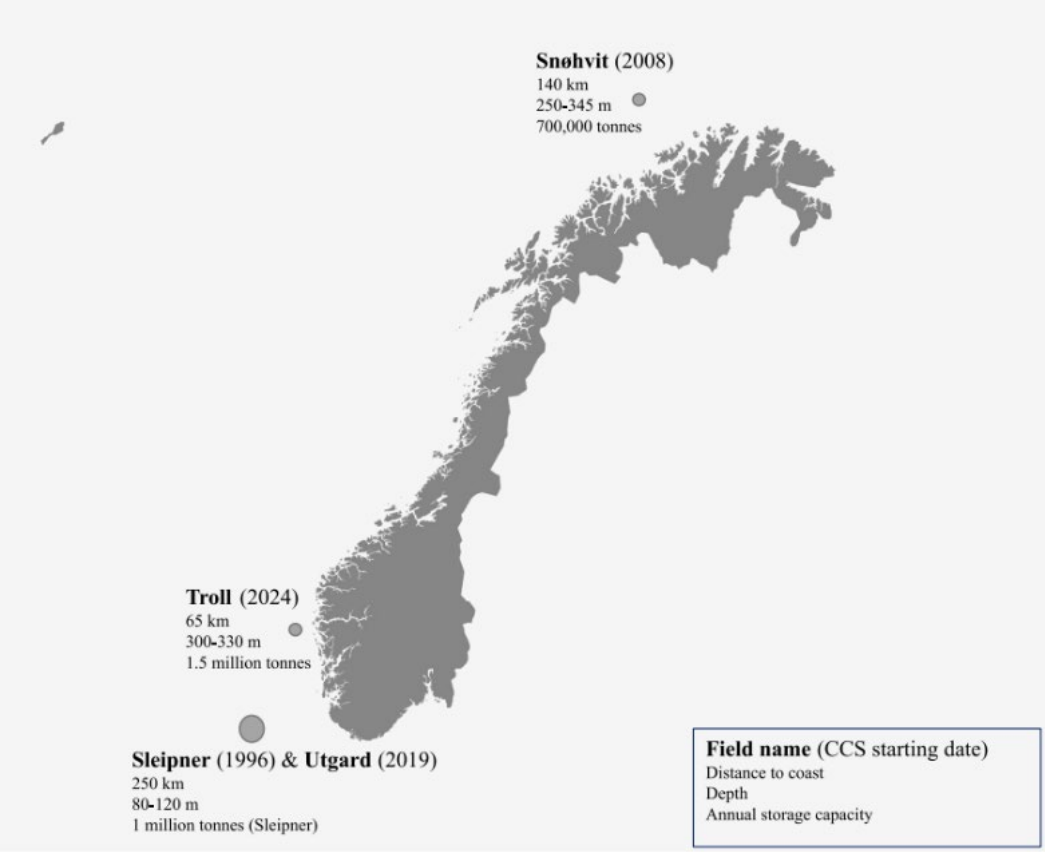

Figure 2 CCS sites at Norwegian Continental Shelf the baseline SST is designed for [4].

Table 1 Main design parameters of the baseline SST

Parameter	**Value**	**Unit**
Length	164	m
Beam	17	m
Weight	3.36×10^7	kg
Center of buoyancy $[x_b, y_b, z_b]$	[0, 0, -0.41]	m
Skeg position x_s	67	m
Skeg area A_S	40	m^2
Forward tunnel thruster position x_{tf}	60	m
Aft tunnel thruster position x_{ta}	-60	m
CO_2 cargo capacity	1.7×10^6	kg

During offloading, the SST will first approach and hover above the area close to the subsea well at operating depth. An ROV will then carry the flexible flowline from the subsea well to the SST for mating. The SST will then offload its CO_2 via the flexible flowline. Finally, the ROV will disconnect the flowline after offloading is complete. This offloading sequence is illustrated in Figure 3. Throughout this process, the SST will maintain its position dynamically using its propeller and thrusters while being subjected to the environmental loads from ocean currents,

as illustrated in Figure 4. The position is controlled using a Linear Quadratic Regulator (LQR) control system designed and tuned in Ma et al. [9].

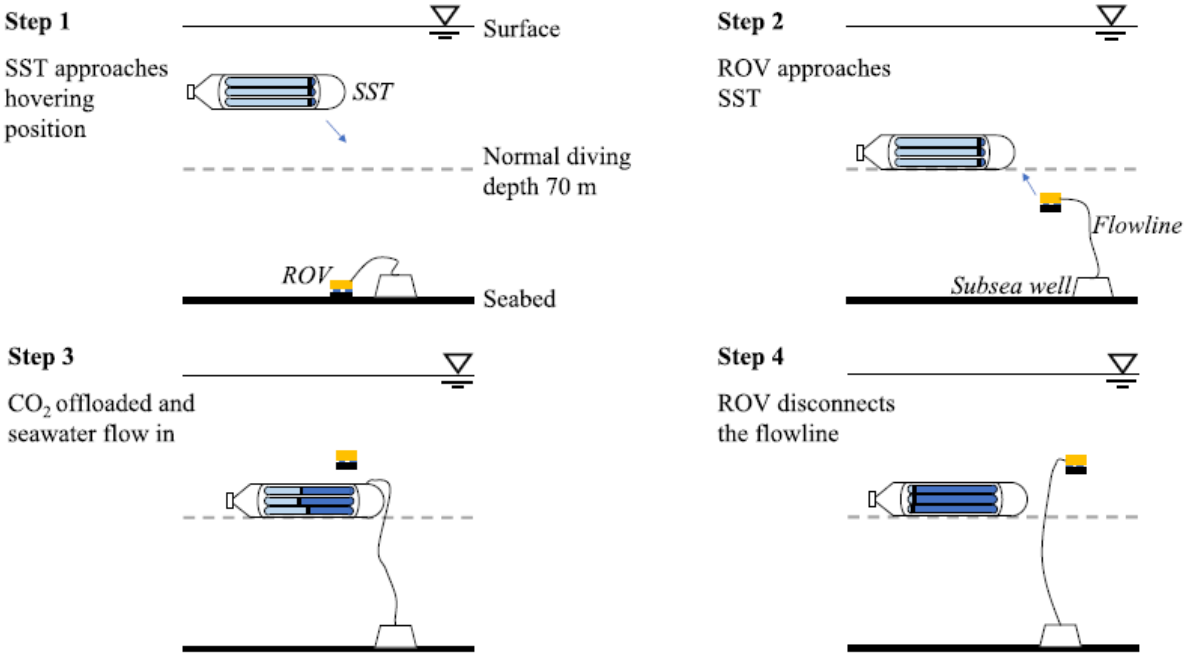

Figure 3 SST offloading sequence [4].

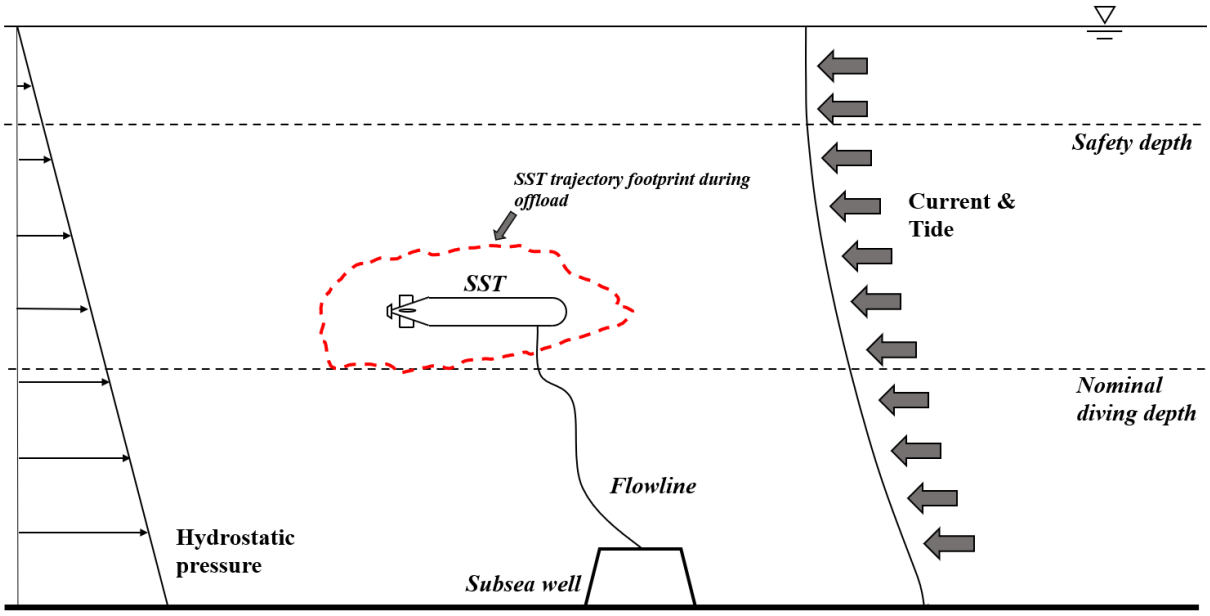

Figure 4 SST subjected to environmental loads during offloading.

Knowing the extreme positional responses (extreme surge and heave) is essential. This is because the extreme heave motion gives the maximum depth, determining the extreme hydrostatic load the SST will experience during operation. Hydrostatic loading is a dominating load and drives the collapse design of the SST pressure hulls. Further, the extreme surge motion

will determine the length of the flowline required to avoid it being taut and resulting in snap loadings. In this paper, the extreme positional responses of the SST as illustrated in Figure 4 as the trajectory footprint (dotted red line) during offloading when the aft thruster fails is investigated for mean current velocities of 0.5, 1.0, and 1.5 m/s using the average conditional exceedance rate (ACER) method based. The empirical data is generated using time-domain simulations with a 2D planar Simulink model.

2. 2D planar model

2.1. Coordinate system

The vehicle body-fixed coordinate system locates at the SST's centre of gravity. The motion of the body-fixed frame of reference is relative to an earth-fixed reference frame (North, East and Down). The centre of buoyancy (CoB) location is right above the centre of gravity. The CoB is also at the geometric centre of the SST. The coordinate system is presented in Figure 5.

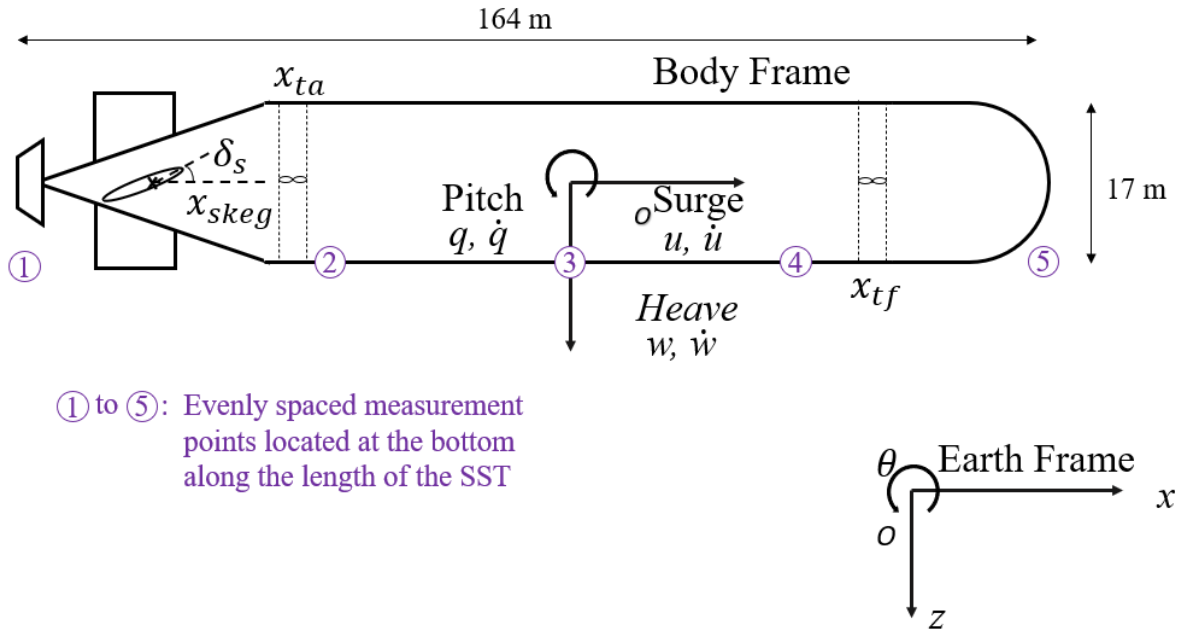

Figure 5 SST coordinate system with measurement points.

2.2. Simulink implementation

The Simulink model is presented in Figure 6 and Figure 7 and is briefly discussed in this sub-section. The model was initially developed by Ma et al. [10] to study the depth control problem and later extended in Ma et al. [9] to include more details on the thrusters, ballast tanks, control system and current loads.

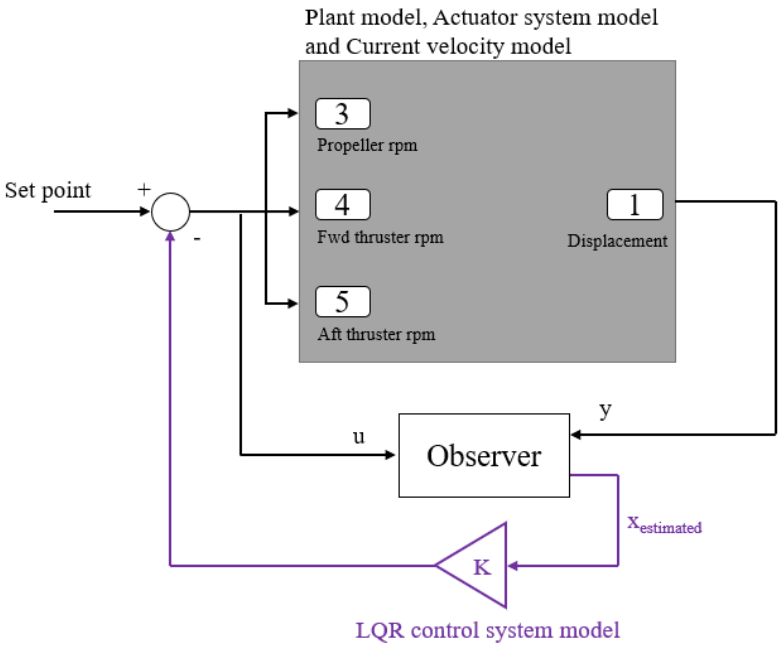

Figure 6 Simulink model implementation – Control system model feedback loop.

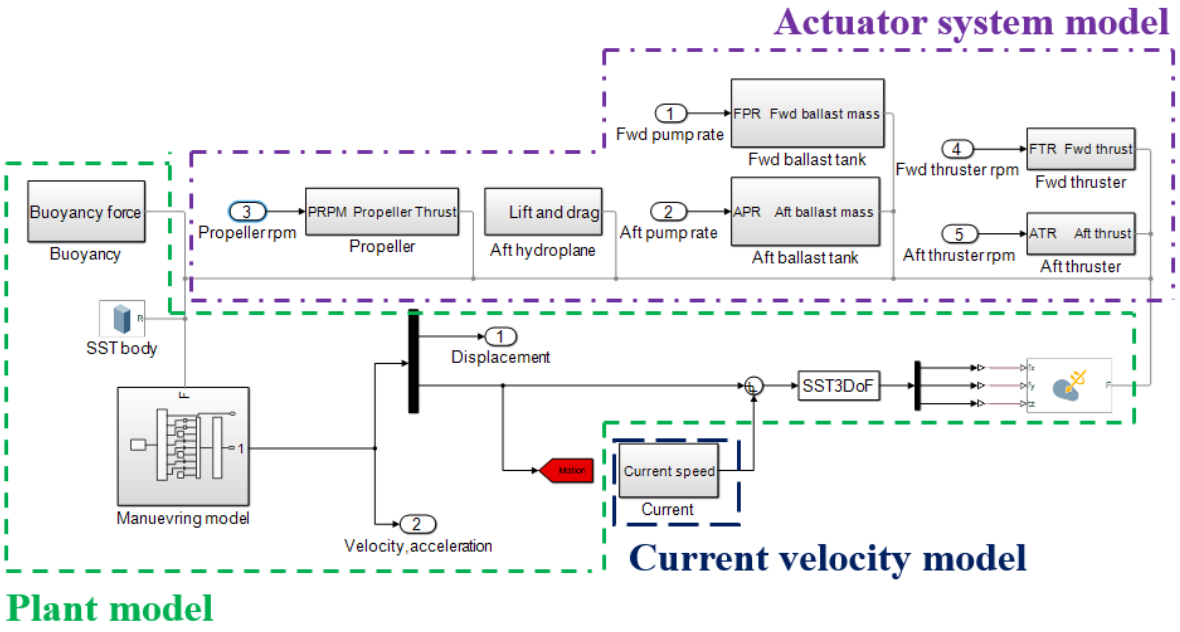

Figure 7 Simulink model implementation – Plant model, Actuator system model and Current velocity model.

The Simulink model consists of the following blocks:

- Plant model: This model implements the equation of motions of the SST considering hydrostatics, hydrodynamic derivatives, body drag forces and body lift forces.
- Actuator system model: This model implements the forces and moments resulting from the ballast tanks, the propeller, and thrusters.
- LQR control system model: This model implements the LQR control system.

- Observer: This implements the Luenberger Observer [11].
- Current velocity model: This model generates the ocean current velocities.

2.3. Plant model

The equations of motion are presented in Eq. (1) for the x, z, and q directions, respectively.

$$\begin{aligned} W(\dot{u} + wq) &= F_x + F_p \\ W(\dot{u} - uq) &= F_z + F_{tf} + F_{ta} + F_s \\ I_{yy}\dot{q} &= M + M_{hs} + M_{tf} + M_{ta} + M_s \end{aligned} \quad (1)$$

where W is mass of the SST, u is the surge velocity in the SST body frame, w is the heave velocity in the SST body frame, q is the pitch angular velocity, F_x is the added and damping force in the surge direction, F_p is the propeller thrust force, F_z is the added mass and damping force in the heave direction, F_{tf} is the fore thruster force, F_{ta} is the aft thruster force, F_s is the skeg force, I_{yy} is the pitch moment of inertia, M is the added mass and damping moment in pitch direction, M_{hs} is the hydrostatic restoring moment in pitch, M_{tf} is the pitch moment generated by the fore thruster, M_{ta} is the pitch moment generated by the aft thruster and M_s is skeg pitch moment. M_{hs} is calculated using Eq. (2).

$$M_{hs} = z_b W g \sin\theta \quad (2)$$

where z_b is the location of the centre of buoyancy (CoB), g is the gravitational acceleration, and θ is the pitch angle of the SST.

The drag and lift forces and moment acting on the SST body, F_x, F_z and M from Eq. (1) are computed using Eq. (3).

$$\begin{aligned} F_x &= X_{\dot{u}}\dot{u} + X_{|u|u}|u|u + X_{wq}wq + X_{qq}q^2 \\ F_z &= Z_{\dot{w}}\dot{w} + Z_{\dot{q}}\dot{q} + Z_{uw}uw + Z_{|w|w}|w|w + Z_{|q|q}|q|q + Z_{uq}uq \\ M &= M_{\dot{q}}\dot{q} + M_{\dot{w}}\dot{w} + M_{uq}uq + M_{uw}uw + M_{|q|q}|u|u + M_{|w|w}|w|w \end{aligned} \quad (3)$$

where $X_{|u|u}$, $Z_{|w|w}$, and $Z_{|q|q}$ are the cross-flow drag terms, $X_{\dot{u}}$, $Z_{\dot{w}}$, $M_{\dot{w}}$, $M_{\dot{q}}$ and $Z_{\dot{q}}$ are the added mass terms, X_{wq}, X_{qq}, and Z_{uq} are the added mass cross-terms. $M_{|w|w}$ and $M_{|q|q}$ are the cross-flow drag terms, $M_{\dot{w}}$ and $M_{\dot{q}}$ are the added mass terms, M_{uq} is the added mass cross term and fin lift, Z_{uw} and M_{uw} are the body lift and Munk moment. These terms are the hydrodynamic derivatives and are estimated following the procedure presented in Prestero [12] and presented in the following.

The nonlinear axial drag hydrodynamic derivative $X_{|u|u}$ is estimated by Eq. (4):

$$X_{|u|u} = -0.5\rho c_d A_f \quad (4)$$

where c_d is the axial drag coefficient, and A_f is the SST frontal area. $c_d = 0.145$ and $A_f = \pi \cdot (8.5)^2 = 227.0$ m^2. The cross-flow drag terms $Z_{|w|w}$, $Z_{|q|q}$, $M_{|w|w}$, and $M_{|q|q}$ are expressed as follows:

$$
\begin{aligned}
Z_{|w|w} &= -0.5\rho c_{dc} \int_{x_{tail}}^{x_{bow}} 2R(x)\, dx \\
M_{|w|w} &= 0.5\rho c_{dc} \int_{x_{tail}}^{x_{bow}} 2xR(x)\, dx \\
Z_{|q|q} &= 0.5\rho c_{dc} \int_{x_{tail}}^{x_{bow}} 2x|x|R(x)\, dx \\
M_{|q|q} &= -0.5\rho c_{dc} \int_{x_{tail}}^{x_{bow}} 2x^3 R(x)\, dx
\end{aligned}
\qquad (5)
$$

where d_{dc} is the cross flow drag coefficient of a cylinder, x_{tail} is SST tail end position, x_{bow} is SST bow position, $R(x)$ is the SST hull radius at corresponding x position. $d_{dc} = 1.1$ (Ref. Hoerner [13]), $x_{tail} = -75.3$ m, and $x_{bow} = 88.7$ m.

Blevins [14] provided an empirical formula for estimating the added mass of an ellipsoid. This is used to obtain the SST axial added mass, $X_{\dot{u}}$ and given as follows:

$$
X_{\dot{u}} = -\frac{4\alpha\pi\rho}{3}\left(\frac{l_{sst}}{2}\right)\left(\frac{d_{sst}}{2}\right)^2 \qquad (6)
$$

where α is an empirical parameter, l_{sst} is the SST length, and d_{sst} is the SST diameter at the parallel mid-body. $\alpha = 0.021$, $l_{sst} = 164$ m and $d_{sst} = 17$ m. From Newman [15], the added mass of a circle slice, $m_a(x)$, can be calculated by Eq. (7).

$$
m_a(x) = \pi\rho R(x)^2 \qquad (7)
$$

As a result, the cross-flow added mass terms could be expressed as:

$$
\begin{aligned}
Z_{\dot{w}} &= -\int_{x_{tail}}^{x_{bow}} m_a(x)\, dx \\
M_{\dot{w}} &= \int_{x_{tail}}^{x_{bow}} x m_a(x)\, dx \\
Z_{\dot{q}} &= M_{\dot{w}} \\
M_{\dot{q}} &= -\int_{x_{tail}}^{x_{bow}} x^2 m_a(x)\, dx
\end{aligned}
\qquad (8)
$$

The cross term hydrodynamic derivatives are obtained from the added mass coupling. They are presented as follow:

$$X_{wq} = Z_{\dot{w}}$$
$$X_{qq} = Z_{\dot{q}}$$
$$Z_{uq} = -X_{\dot{u}}$$
$$M_{uq} = -Z_{\dot{q}}$$
$$M_{uw_a} = -(Z_{\dot{w}} - X_{\dot{u}})$$

(9)

The SST body lift and lift moment can be expressed as follows:

$$Z_{uw} = -0.5\rho d^2 c_{yd\beta}$$
$$M_{uw_l} = -0.5\rho d^2 c_{yd\beta} x_{cp}$$

(10)

where $c_{yd\beta}$ is the Hoerner lift slope coefficient, and x_{cp} is the x position of the viscous force centre. $c_{yd\beta}$=0.003 (Ref. Prestero [12]) and x_{cp}= -31.6 m (Ref. Hoerner [13]).

Finally, the pitch moment cross term M_{uw} can be expressed as:

$$M_{uw} = M_{uw_a} + M_{uw_l}$$

(11)

2.4. Actuator system model

The actuator system consists of the ballast tanks, the propeller, skegs, and thrusters. These are discussed in the following sub-sections.

Ballast tanks

The neutral buoyant and trim condition is maintained using the ballast tanks divided into the compensation tanks and the trim tanks. Two compensation tanks located at the fore and aft provide the trim moment and weight necessary to achieve neutral buoyancy. Further, two trim tanks that are smaller than the compensation tanks are located at the fore and aft. They provide the finer adjustments required to ensure that the CoG is vertically below the CoB. This helps to maintain the neutral trim condition. In addition to the ballast tanks, the buoyancy tanks also provide additional ballasting capacity to assist in the SST staying neutral buoyant. The locations of these tanks are presented in the general arrangement shown in Figure 8.

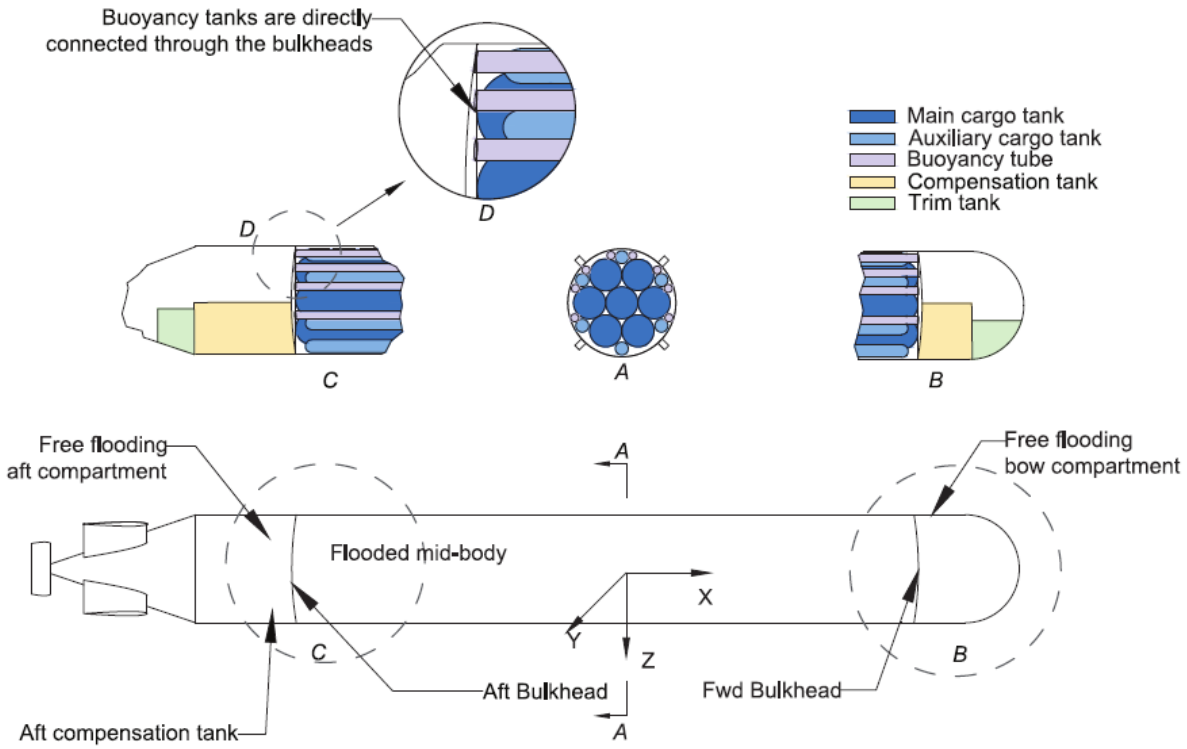

Figure 8 Tank arrangement of the SST [4].

Propeller

The SST uses a three-bladed Wageningen B-series propeller [16] with a diameter, d_p of 7 m and a blade area ratio of 0.3. This results in a propeller thrust coefficient, K_{Tp} = 0.19. The propeller thrust force, F_p acting on the SST, is given as:

$$F_p = \rho K_{Tp}^2 n_p d_p^4 \quad (12)$$

where ρ is the seawater density, and n_p is the propeller rotational speed in rad/s.

Skegs

The pitch motion and depth of the SST are controlled by four skegs located at the starboard and port side of the aft. There are two skegs on each side. The force and pitch moment, F_s and M_s acting on the SST, respectively is given as:

$$F_s = 0.5\rho C_L S_{skeg} \delta_s u^2 \qquad M_s = x_{skeg} F_s \quad (13)$$

where C_L is the skeg's lift rate coefficient, S_{skeg} is the skeg area, δ_s is the skeg angle, u is the effective inflow velocity and x_{skeg} is the axial position of the fin post in the SST body frame. C_L = 6.102 rad/s from Ma et al. [5] is used. This C_L value is based on a hydrodynamic XFOIL evaluation [17] of Bower's airfoil profile [18] subjected to a flow with Re = 5 x 10^6. S_{skeg} = 40 m^2, δ_s = 0 ° and x_{skeg} = 67 m are used.

Thrusters

There are one fore and one aft thruster; both thrusters are identical. The thruster force and resulting pitch moment acting on the SST, F_t and M_t are given in Eq. (14) and (15), respectively.

$$F_t = \rho K_{Tt}^2 n_t d_t^4 \quad (14)$$

$$M_t = F_t x_t \quad (15)$$

where K_{Tt} is the thrust coefficient, ρ is the water density, n_t is the thruster rotational speed, d_t is the thruster diameter, and x_t is the location of the thruster on SST. K_{Tt} = 0.4, ρ = 1025 kg/m^3, d_t = x m and x_t = -60 m and 60 m (fore thruster and aft thruster, respectively) are used.

2.5. LQR control system model

The linear quadratic regulator (LQR) is a well-known design technique that provides optimally controlled feedback gains and is used in this paper. LQR has been a popular choice when it comes to underwater vehicles. It has been utilized for the depth-control of autonomous vehicles [22] and steering control [23]. The LQR method uses the state space equation system of the SST for deriving the required gains. This controller stabilizes the system using full state feedback. The state space equation can be written as:

$$\dot{x} = Ax + Bu \qquad y = Cx \quad (16)$$

where A is the state matrix, B is the input matrix, C is the output matrix, x is the state vector, u is the input vector, and y is the output vector. The calculation of the state space matrices is further described in Section 2.5.1.

The optimal gain matrix of the LQR is found as a balance of the performance of the system and the actuator effort. A state-feedback controller u = -Kx is designed where K is the optimal

feedback control gain matrix. Its purpose is to minimize the infinite horizon quadratic cost function J defined as:

$$J = \int_0^\infty (x^T Q x + u^T R u) dt \quad (17)$$

where Q is the state weighting matrix and R is the energy weighting matrix, which determines the importance of state error and energy expenditure, respectively. The controller is tuned by adjusting the weights of Q and R and is described further in Section 2.5.2.

2.5.1. Linearized state space model

Ma et al. [9] found that tuning for a 1 ° heading is appropriate for the head-on ocean current case, which this paper investigates. The model linearizer in Matlab is used. The inputs of the linearized model are [n_p; n_{tf}; n_{ta}]. The outputs are [x; z; θ]. The state space matrices, A and B, are calculated using linearization at the operating point of the steady current velocity of 0.5, 1 and 1.5 m/s, respectively, for the individual mean current velocity cases (Ref Section 4) at a heading of 1 °. This gives a 6 by 6 A, 6 by 3 B matrix, and a 3 by 6 C matrix as presented in Eq. (18) for the 1 m/s current velocity case.

$$A = \begin{bmatrix} 0 & 0 & 0 & & 1 & 0 & 0 & \\ 0 & 0 & 0 & & 0 & 1 & 0 & \\ 0 & 0 & 0 & & 0 & 0 & 1 & \\ 0 & 0 & -2.65\times10^{-5} & -1.00\times10^{-3} & 1.21\times10^{-4} & -0.0145 \\ 0 & 0 & -2.87\times10^{-6} & -1.32\times10^{-4} & -0.0089 & 0.0518 \\ 0 & 0 & -0.0237 & -6.21\times10^{-5} & 0.0039 & -0.0596 \end{bmatrix}$$

$$B = \begin{bmatrix} 0 & 0 & 0 \\ 0 & 0 & 0 \\ 0 & 0 & 0 \\ 2.54\times10^{-10} & 8.80\times10^{-5} & 4.24\times10^{-10} \\ 3.84\times10^{-6} & -5.25\times10^{-9} & 6.40\times10^{-6} \\ 7.13\times10^{-7} & 0 & -1.19\times10^{-6} \end{bmatrix}$$

$$C = \begin{bmatrix} 1 & 0 & 0 & 0 & 0 & 0 \\ 0 & 1 & 0 & 0 & 0 & 0 \\ 0 & 0 & 1 & 0 & 0 & 0 \end{bmatrix} \quad (18)$$

2.5.2. Control tuning

The LQR controller is tuned based on the state-space matrices A and B. The SST is tuned by adjusting the weights of Q and R matrices. This iterative process does not follow any hard and fast rules or any strict technique. A complete understanding of the system dynamics is a must to tune the weights. Response time should be observed compared to the system's desired performance, allowing the designer to fine-tune the weights. The 22-coefficient and 33-coefficient of the R matrix represent the efforts applied by the aft and fore thrusters. In this case, the 22-coefficient is set to 10^{-5} to represent a failure in the aft thruster. The Q and R matrices

were studied in Ma et al. [9] for the SST hovering in the current problem and provided good system responses. These are presented in Eq. (19) and are used in this paper.

$$Q = \begin{bmatrix} 1 & 0 & 0 & 0 & 0 & 0 \\ 0 & 1 & 0 & 0 & 0 & 0 \\ 0 & 0 & 1 & 0 & 0 & 0 \\ 0 & 0 & 0 & 1 & 0 & 0 \\ 0 & 0 & 0 & 0 & 1 & 0 \\ 0 & 0 & 0 & 0 & 0 & 1 \end{bmatrix}; R = \begin{bmatrix} 0.01 & 0 & 0 \\ 0 & 10^{-5} & 0 \\ 0 & 0 & 1 \end{bmatrix} \quad (19)$$

The Q and R matrices in Eq. (19) leads to the following K matrix presented in Eq. (20) for the 1 m/s current velocity case.

$$K = \begin{bmatrix} 0.61 & 98.49 & -260.35 & 0.042 & 5.15 \times 10^{3} & 121.56 \\ 315.61 & -196.87 & 304.40 & 2.69 \times 10^{3} & -6.01 \times 10^{3} & -481.54 \\ 0.0102 & 1.62 & -4.31 & 7.86 \times 10^{-4} & 85.29 & 1.98 \end{bmatrix} \quad (20)$$

2.6. Observer

The discrete-time Luenberger Observer [11] is used in this paper to estimate the states of the SST. The observer implements the following discretised equation:

$$\hat{x}(k+1) = A_d\hat{x}(k) + B_d u(k) + L_d\big(y(k) - \hat{y}(k)\big) \quad (21)$$

where $\hat{x}(k)$ is the kth estimated state vector, $\hat{y}(k)$ is the kth estimated output vector, $u(k)$ is the kth input vector, $y(k)$ is the kth measure output vector, A_d is the discretised state matrix, B_d is the discretised input matrix and L_d is the discretized observer gain matrix. The A_d and B_d matrices used are the A and B matrices obtained from the linearized model presented in Section 2.5.1. L_d is chosen based on a pole placement study presented in Ma et al. [9] and is shown in Eq. (22).

$$L_d = \begin{bmatrix} 4818 & 179 & 33 & 53003 & 2034 & 331 \\ 114 & -1373 & 982 & 1049 & 11826 & 43893 \\ -211 & 2336 & -1672 & -2200 & 25260 & -50749 \end{bmatrix} \quad (22)$$

2.7. Current velocity model

The ocean current velocity, V_c and current inflow angle θ_c are generated using a first-order Gauss-Markov process [19], [20]:

$$\begin{aligned} \dot{V}_c + \mu_1 V_c &= \omega_1 \\ \dot{\theta}_c + \mu_2 \theta_c &= \omega_2 \end{aligned} \quad (23)$$

where μ_1 and μ_2 are constants that determine the time constant of the Gauss-Markov process and is a non-negative value according to Fossen's recommendation [19]. ω_1 and ω_2 are

Gaussian white noises. In this study, a small value $\mu_1 = \mu_2 = 1$ is used to generate a steady state current. The noise power of ω_1 and ω_2 is set to be 0.1 to render the fluctuating part in current velocity and current direction. The design current velocity for the SST is 1 m/s which is the highest observed current velocity at the Norwegian coastal [21].

The current velocities in the surge and heave directions (SST body frame) are then calculated as:

$$u_c = V_c \cos\theta_c$$
$$w_c = V_c \sin\theta_c \qquad (24)$$

where u_c and w_c are the water velocities in the x and z directions, respectively. The incoming water velocity experience by the SST, u and w in the surge and heave directions (SST body frame) are calculated as follows:

$$u = u_{sst} - u_c$$
$$w = w_{sst} - w_c \qquad (25)$$

where u_{sst} and w_{sst} are the velocities of the SST in the surge and heave directions (SST body frame).

3. Averaged conditional exceedance rate (ACER) method

Consider a long term global response process $X(t)$ of the submarine hull, measured over a time interval $(0, T)$. Let $X_1, \dots, X_N$ be measurements of the process $X(t)$ at discrete points in time $t_1, \dots, t_N$ in $(0, T)$. The target is to estimate the distribution function of the extreme value $M_N = \max\{X_j ; j = 1, \dots, N\}$ accurately namely, to estimate CDF (cumulative density function) $P(\eta) = \text{Prob}(M_N \leq \eta)$ for large values of the response η. The following random functions are introduced:

$$A_{kj}(\eta) = \mathbf{1}\{X_j > \eta, X_{j-1} \leq \eta, \dots, X_{j-k+1} \leq \eta\}, \qquad j = k, \dots, N, k = 2, 3, \dots \qquad (26)$$

and

$$B_{kj}(\eta) = \mathbf{1}\{X_{j-1} \leq \eta, \dots, X_{j-k+1} \leq \eta\}, \qquad j = k, \dots, N, k = 2, 3, \dots, \qquad (27)$$

where $\mathbf{1}\{\mathcal{A}\} = 1$ if $\mathcal{A}$ is true, while it is 0 if not. As shown in [24] - [28]:

$$P_k(\eta) \approx \exp\left(-\sum_{j=k}^{N} \frac{\mathbb{E}[A_{kj}(\eta)]}{\mathbb{E}[B_{kj}(\eta)]}\right) \approx \exp\left(-\sum_{j=k}^{N} \mathbb{E}\left[A_{kj}(\eta)\right]\right), \qquad \eta \to \infty \qquad (28)$$

The measured time series can be subdivided into K subsequent (short term) blocks such that $\mathbb{E}[A_{kj}(\eta)]$ remains approximately constant within each block and such that $\sum_{j\in C_i}\mathbb{E}\left[A_{kj}(\eta)\right] \approx \sum_{j\in C_i} a_{kj}\,(\eta)$ for a sufficient range of η-values, where C_i stands for the set of indices for the block with number i; with $i = 1, \ldots, K$, and where $a_{kj}(\eta)$ are the realized values of $A_{kj}(\eta)$ for the measured time series, then $\sum_{j=k}^{N}\mathbb{E}\left[A_{kj}(\eta)\right] \approx \sum_{j=k}^{N} a_{kj}\,(\eta)$. Thus, for a given long term response process, one can write

$$P_k(\eta) \approx \exp\left(-(N-k+1)\hat{\varepsilon}_k(\eta)\right), \qquad (29)$$

where

$$\hat{\varepsilon}_k(\eta) = \frac{1}{N-k+1}\sum_{j=k}^{N} a_{kj}\,(\eta)\,. \qquad (30)$$

In the above equations, an assumption of ergodicity has been used for each short term segment of the recorded time series in order to estimate the short term expected values by using observed values of the $a_{kj}(\eta)$ functions. An alternative way of expressing the long term extreme value distribution in Eq. (29), is obtained by considering the empirical probability distribution of $m = 1,..,M$ sea current states having probabilities p_m, so that $\sum_{m=1}^{M} p_m = 1$. Next, introduce the long term ACER function of order k

$$\mathrm{ACER_k}(\eta) \equiv \sum_{m=1}^{M} \hat{\varepsilon}_k(\eta, m)\, p_m \qquad (31)$$

where $\hat{\varepsilon}_k(\eta, m)$ has the same expression as in Eq. (30) but restricted to the specific sea state with number m. As shown in [24] - [28], the long-term extreme value distribution of $M(T)$, can then be expressed as follows based on the ACER function of order *k*:

$$P(\eta) \approx \exp\left(-N\cdot\mathrm{ACER_k}(\eta)\right) \qquad (32)$$

where $ACER_k(\eta)$ is the long term empirical ACER function of order *k*, with $k \ll N$; N is the total number of data points from the recorded time series used in the estimation of the ACER functions. Typically, this could be local peaks from the measured time series.

As the order *k* increases, the accuracy of Eq. (32) improves; results from Section 0 ????? of this paper show that the $\mathrm{ACER_k}(\eta)$ functions converge conveniently fast with growing *k*, see [24] - [28]. Note that by increasing the conditioning level *k*, possible data clustering effects, e.g. with narrow-band response components in the recorded time series, can be accounted for. This

is an essential advantage of ACER method as it increases the accuracy of its extreme predictions and avoids resulting in over-conservative design values.

The $ACER_k$ as functions of the level η are generally quite regular in the tail, i.e., for high response values of η. More specifically, for $\eta \geq \eta_0$, the tail behaves very closely like $\exp\{-(a\eta + b)^c + d\}$ with a, b, c, d being suitable constants.

It is suggested to do the optimization on the log-level by minimizing the following mean square error function F with respect to the four arguments a_k, b_k, c_k, p_k, q_k.

$$F(a_k, b_k, c_k, p_k, q_k) = \int_{\eta_0}^{\eta_1} \omega(\eta) \left\{\ln\left(\mathrm{ACER_k}(\eta)\right) - d_k + (a_k\eta + b_k)^{c_k}\right\}^2 d\eta, \quad \eta \geq \eta_0 \qquad (33)$$

where η_1 is a suitable data cut-off value, i.e. the largest η response value with a confidence interval with acceptable interval width. The weight function ω is defined as $\omega(\eta) = \{\ln C^+(\eta) - \ln C^-(\eta)\}^{-2}$ with $\left(C^-(\eta),\ C^+(\eta)\right)$ being a 95% CI, empirically estimated from the measured data. A detailed procedure for further optimizing parameters a_k, b_k, c_k, d_k has been outlined in [24] - [28].

4. Case studies

Three mean current velocities of 0.5, 1.0 and 1.5 m/s are studied in this paper. A total of 20 4-hour simulations is performed for each mean current velocity, i.e., there is a total of 60 4-hour simulations performed in this paper. The responses at the five measurement points presented in Figure 4 are considered. These are five evenly spaced points located at the bottom along the length of the SST.

5. Results and discussions

This paper presents the methodology for estimating the SST's extreme responses hovering in ocean current during offloading when the aft thruster fails. The empirical data is based on accurate numerical simulations using a Simulink model as presented in Section 2. The ACER2D (bivariate averaged conditional exceedance rate) method is presented in Section 3. The proposed methodology provides an accurate bivariate extreme value prediction, utilizing all available data efficiently. Based on the overall performance of the proposed method, it was concluded that the ACER2D method could incorporate environmental input and provide a more robust and accurate bivariate prediction based on proper numerical simulations. For a detailed definition of ACER1D and ACER2D functions, see [24] - [28].

The described approach may be used at the SST design stage to provide the opportunity of defining optimal vessel motion control parameters that would minimize potential vessel damage.

5.1. Time-domain responses

Figure 9 presents R_1 and R_5 displacement responses simulated time series. R_1 and R_5 are the locations at the aft and fore of the bottom of the SST, respectively, as illustrated in Figure 5. Each time record is 80 hours, comprising 20 independent 4-hour time series. It is seen that response R_5 possesses asymmetric behaviour with respect to its upper and lower bounds. The latter indicates more efficient control on the upper response bound.

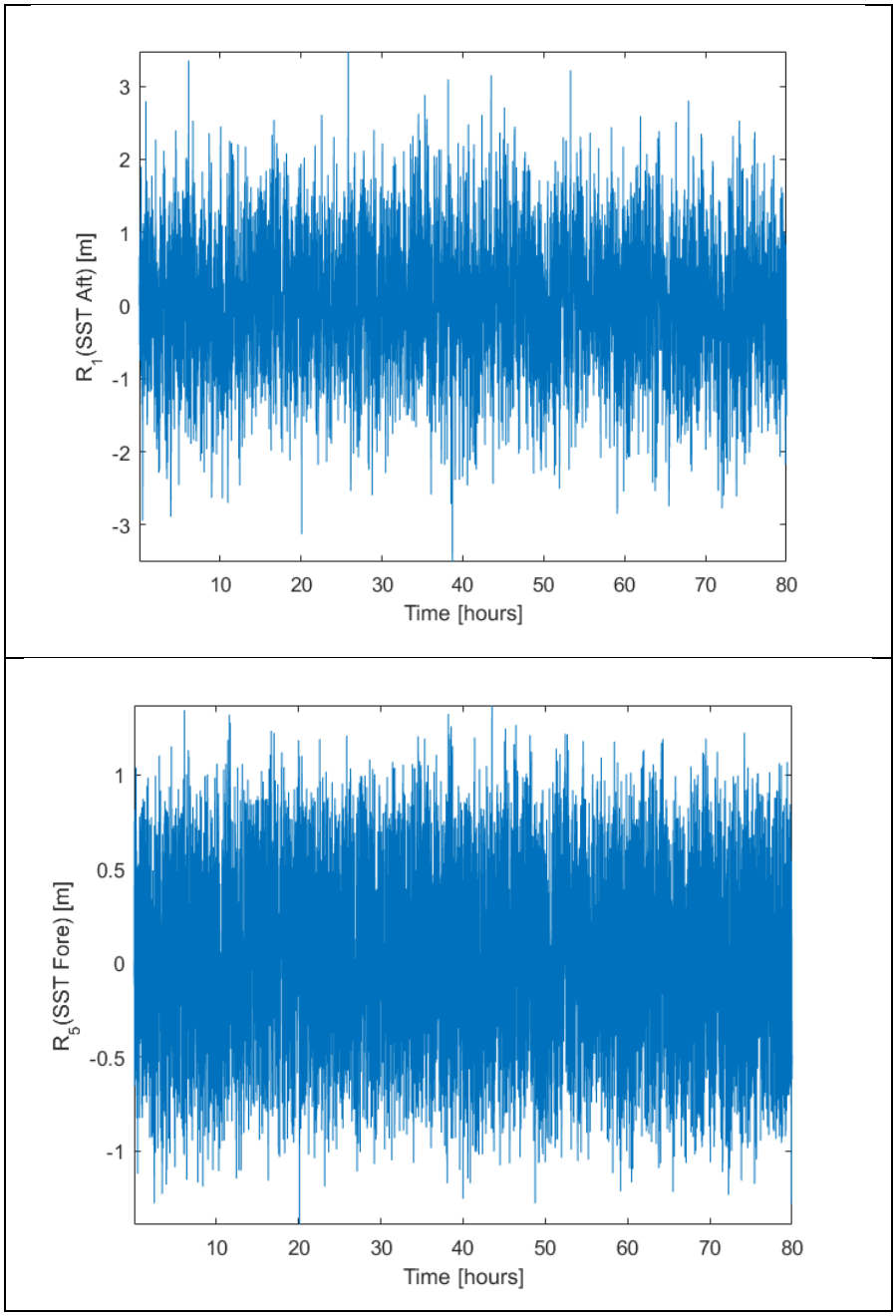

Figure 9 Response time series. Top: R_1 (SST aft); Bottom: R_5 (SST fore). Current speed 0.5 m/s

Figure 10 presents the PSD (power spectral density) of the response R_1. It is seen that there is a PSD peak at the frequency, f of about 0.005 Hz, or equivalently at the eigenperiod, T of about

3 minutes. The latter information should be reflected in the choice of conditioning level *k* of ACER functions, see Section 3.

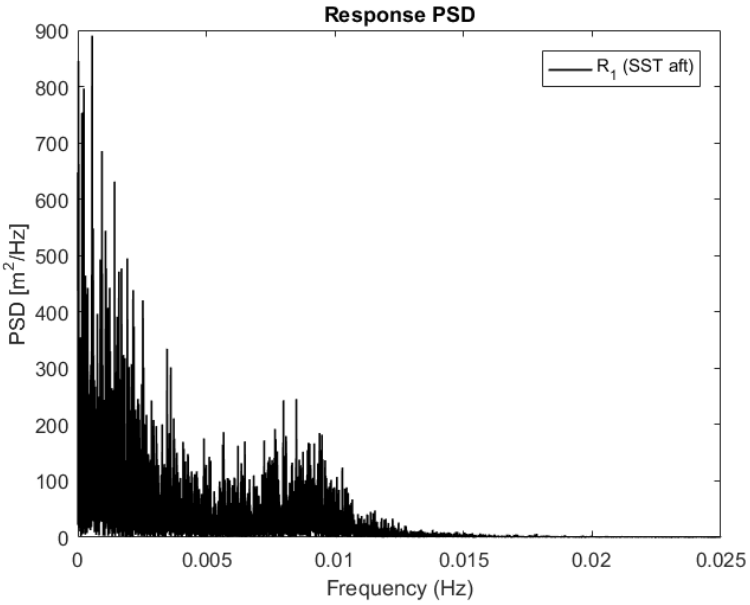

Figure 10 Response R_1 (SST aft) PSD. Current speed = 0.5 m/s

The 4-hour maxima responses for the 20 simulations are presented in Figure 11. As observed, there are differences in the individual 4-hour maxima response in each simulation case. This is an inherent property of all stochastic processes, highlighting the importance of using extreme value prediction methods such as the ACER method to predict longer-term maxima responses used as design characteristic values accurately. In general, the responses at the aft and fore, i.e., R_1 and R_5, are significantly larger than the responses closer to the centre of the SST. The SST aft and fore move more in heave due to the contribution from the pitch motion. Further, the R_1 (SST aft) responses are more significant than the R_5 (SST fore) responses. This is because the aft thruster has failed and is not working. The differences between the R_1 (SST aft) and the R_5 (SST fore) responses increase with decreasing mean current velocities.

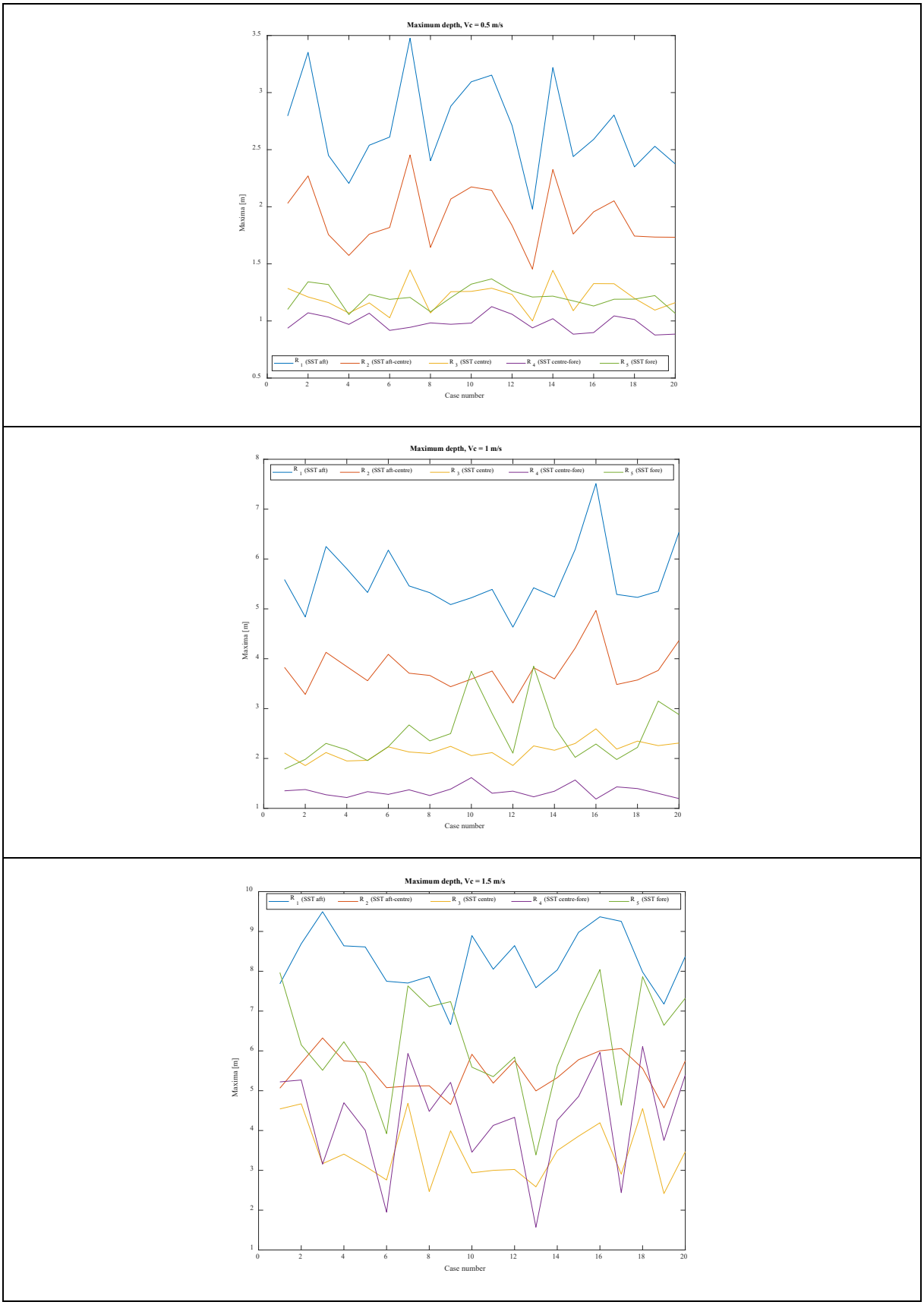

Figure 11 4-hour maxima responses for the 20 simulations. Top: V_c = 0.5 m/s; Middle: V_c = 1 m/s; Bottom: V_c = 1.5 m/s.

The maximum responses corresponding to each current velocity for the 20 4-hour simulations are summarised in Table 2.

Table 2 Maximum SST responses for 20 4-hour simulations

SST response [m]	***Vc* = 0.5 m/s**	***Vc* = 1 m/s**	***Vc* = 1.5 m/s**
R_1 (SST aft)	3.476	7.512	9.495
R_2 (SST aft-centre)	2.454	4.968	6.324
R_3 (SST centre)	1.446	2.594	4.684
R_4 (SST centre-fore)	1.125	1.616	6.109
R_5 (SST fore)	1.368	3.850	8.042

5.2. Extreme responses: univariate and bivariate analysis

This section presents statistical analysis results for R_1 and R_5 displacement responses using the univariate and bivariate methods, i.e. ACER1D and ACER2D, respectively, [24]-[35]. The focus is on the accurate prediction of extreme response, which is vital for safety and reliability at the design stage. The conditioning level k is set to be 50, as it was observed that ACER functions have converged at that level in the distribution tail, see Section 3.

Figure 12 presents univariate extreme response 5-year return period prediction with 95 % confidence interval (CI); the 5-year return period is chosen purely as an example. The predicted extreme probability level is selected as $p = 10^{-9}$. Note that the original 80 hours data set has at most a probability level of about $p = 1/N \approx 2 \cdot 10^{-7}$ with N being the number of discrete time data points in the underlying response time series. Therefore, the probability tail was extrapolated two orders below what the original data contains. Note that probability level, p is inversely related to a return period, T, which can be given, for example, in years. Figure 13 presents the Gumbel plot for R_5. The dashed line indicates extrapolation towards a 5-year return period. The prediction in Figure 13 can be directly compared with Figure 12 (bottom). Although both methods predicted 5-year return period R_5 (SST fore) values of about 1.5 meters, it is seen that Gumbel 20 4-hour maxima points do exactly align into a straight line. This means that the asymptotic generalized extreme value (GEV) condition was not yet developed in the analysed data set. Subsequently, the Gumbel method bootstrapped 95 % CI is substantially wider than the 95 % CI predicted by the ACER method. The much smaller 95 % CI is a clear advantage of the ACER1D method.

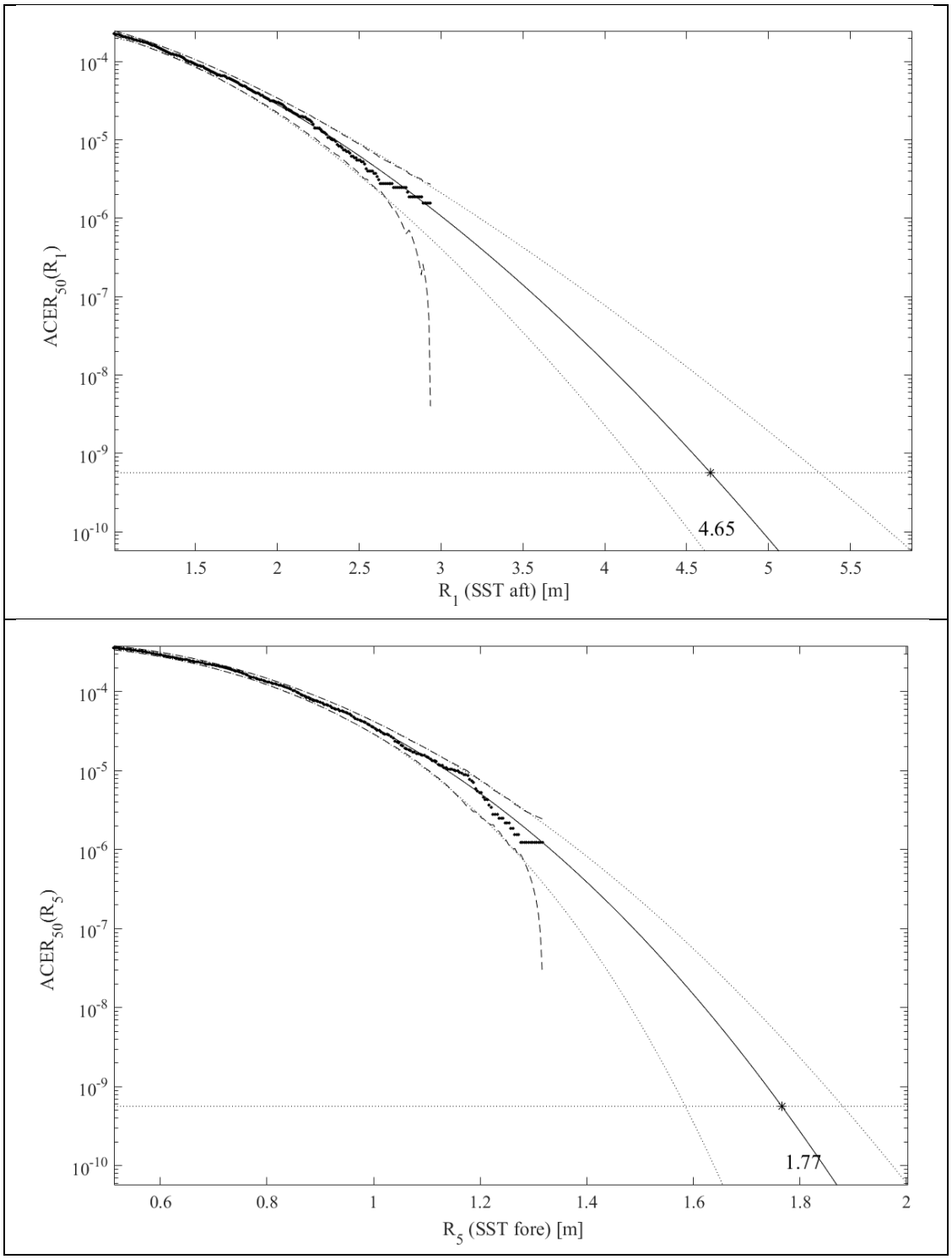

Figure 12 Univariate ACER1D extreme response 5-year prediction with 95% CI (dotted lines). Top: R_1 (SST aft); Bottom: R_5 (SST fore); decimal log scale. Current speed = 0.5 m/s.

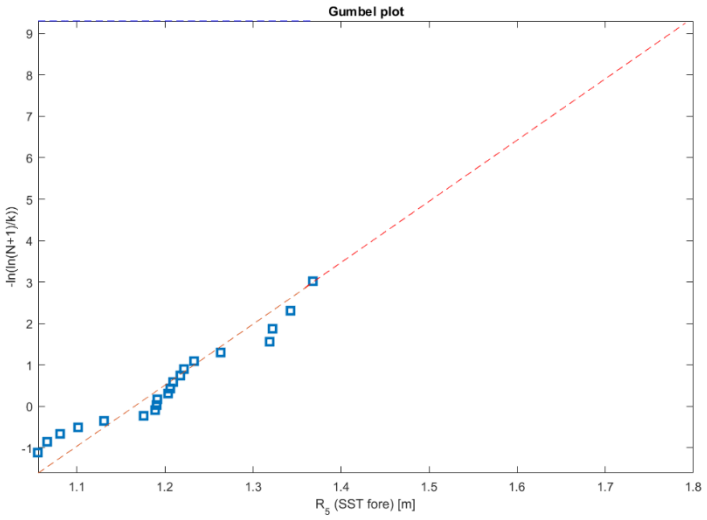

Figure 13 Gumbel plot for R_5 (SST fore), dashed line indicates extrapolation towards a 5-year return period. 20 4-hours maxima points. Current speed = 0.5 m/s.

Figure 14 presents the phase space for responses R_1 (SST aft) vs R_5 (SST fore), along with the bivariate empirical ACER2D function $\hat{\mathcal{E}}_k$ (see Section 3). It is clearly seen that there is a nonlinear correlation between responses R_1 (SST aft) and R_5 (SST fore). The bivariate empirical ACER2D surface, $\hat{\mathcal{E}}_k$ obviously marginally corresponds to univariate ACER1D functions presented in Figure 12.

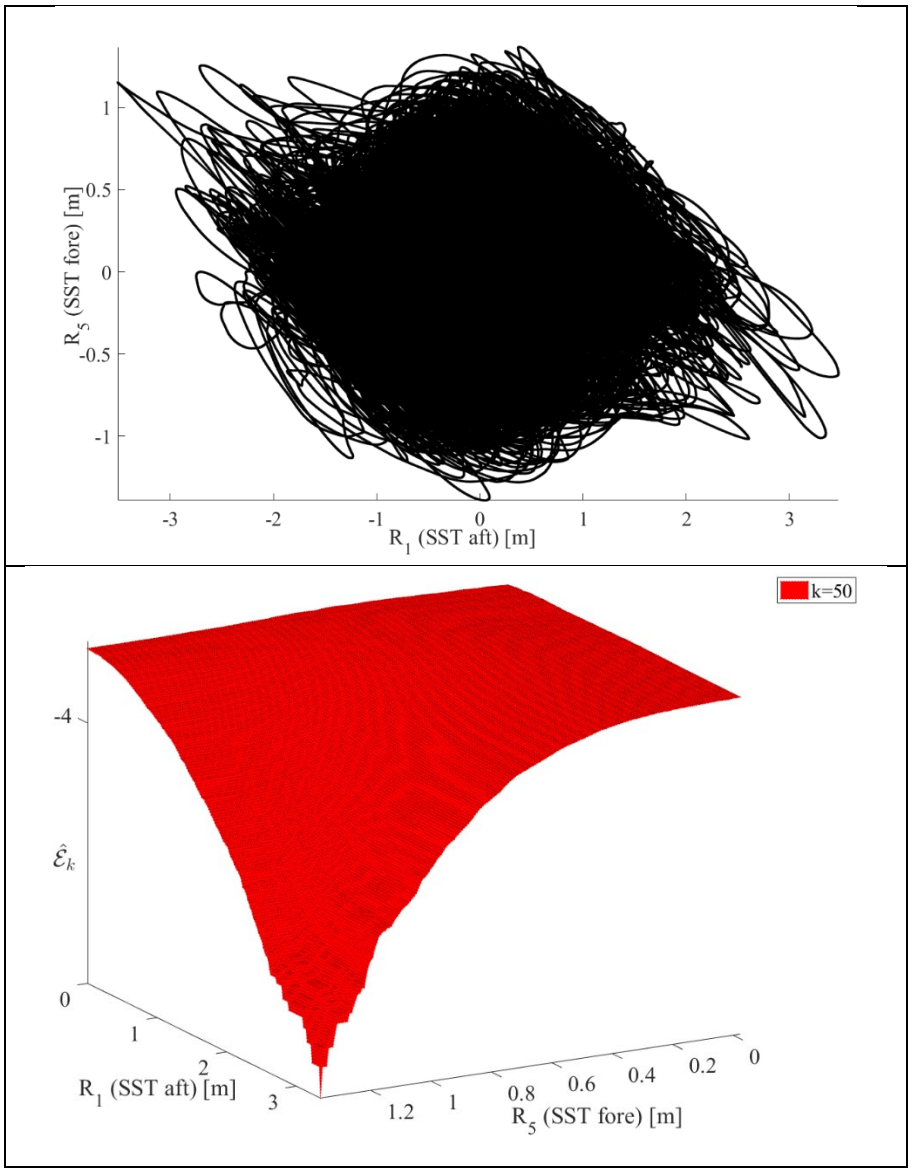

Figure 14 Top: phase space, response R_1 (SST aft) vs R_5 (SST fore); Bottom: bivariate empirical ACER2D function $\hat{\mathcal{E}}_k$, decimal log scale. Current speed = 0.5 m/s.

Figure 15 presents the ACER2D fit to empirical data along with the predicted bivariate contours with return periods in years (on the right). Figure 15 shows the contour lines for the optimized Asymmetric logistic (AL) $\mathcal{A}_k(R_1, R_5)$ and optimized Gumbel logistic (GL) $\mathcal{G}_k(R_1, R_5)$ models, optimally matched to the corresponding empirical bivariate ACER2D function $\hat{\mathcal{E}}_k(R_1, R_5)$, $k = 50$, see Gaidai et al. [29][30][32][33], Gao et al. [31] and Xu et al. [34] for more information on GL and AL definitions. The contour lines negative labelling numbers in Figure 15 indicate decimal logarithmic scale probability levels of $P(R_1, R_5)$. Figure 15 clearly shows that the empirical bivariate ACER2D surface $\hat{\mathcal{E}}_{50}$ well captures the strong correlation between load/response components. The optimized models $\mathcal{G}_{50}$ and $\mathcal{A}_{50}$ exhibit smooth contours along with matching ACER2D empirical contours. The later models may be better suited for the response processes bivariate extreme value distributions. Figure 15 shows good agreement between the estimated optimized AL and GL surfaces and the bivariate ACER2D surface. This means that the correlation between responses R_1 (SST aft) and corresponding R_5 (SST fore) is a crucial non-negligible factor influencing the shape of the bivariate contour lines.

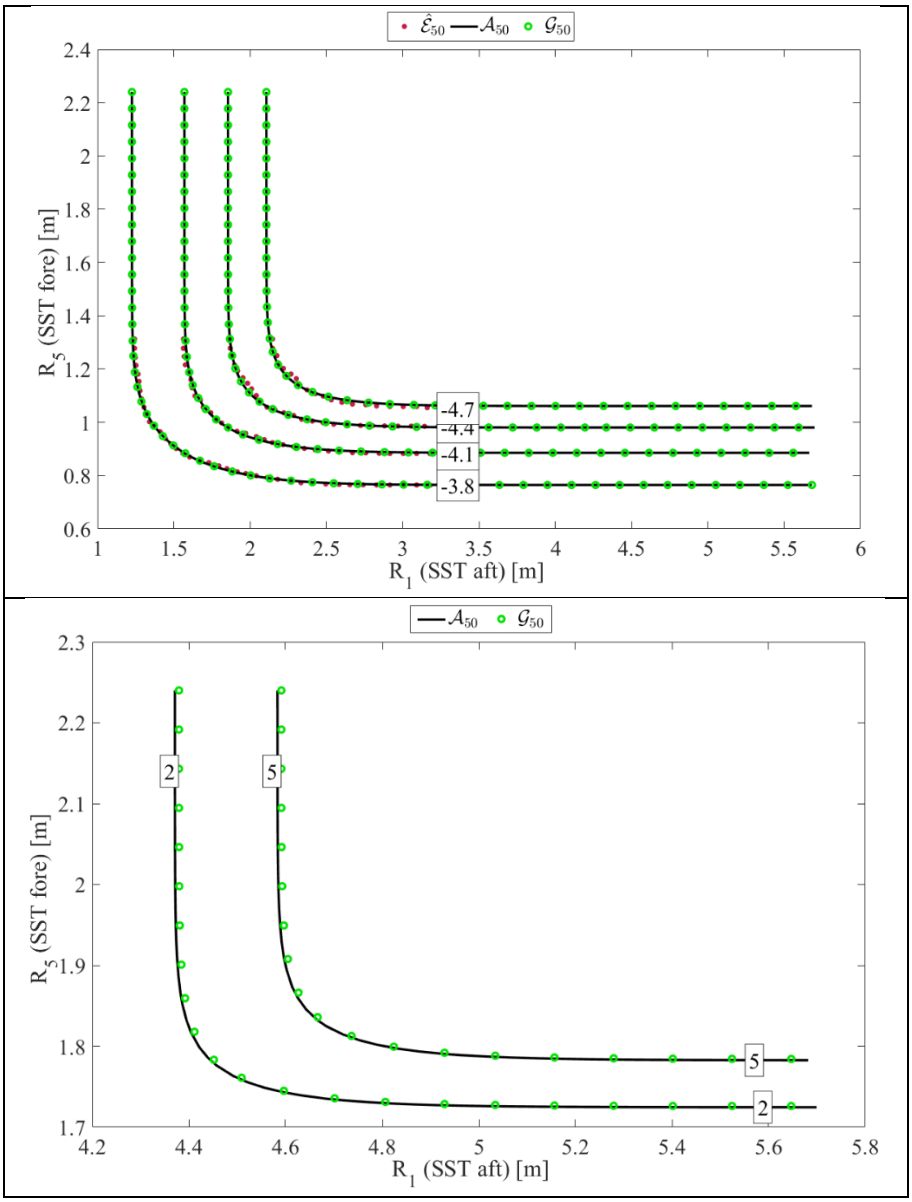

Figure 15 Top: ACER2D fit to empirical data; Bottom: predicted bivariate contours with return periods in years. Current speed = 0.5 m/s.

The lowest probabilities in Figure 14 and Figure 15 correspond to the value N^{-1} where N is the number of equidistant time points in the studied time series, see Eqs. (28) to (32) in Section 3. Figure 15 (bottom) presents the predicted bivariate contours with corresponding return periods of 2 and 5 years. Note that the return period of a few years is quite long compared to the short duration of the analysed measured record. As seen from Figure 15 (bottom), the fitted lines match the empirical data well, highlighting the accuracy of the ACER method. Further the ACER method is efficient as it requires only 20 4-hour realisations to generate accurate results.

Figure 16 shows that the univariate design point lies outside the safe 2-years zone (dashed area) and is outside the 2D design zone. This means that the 1D method is not conservative.

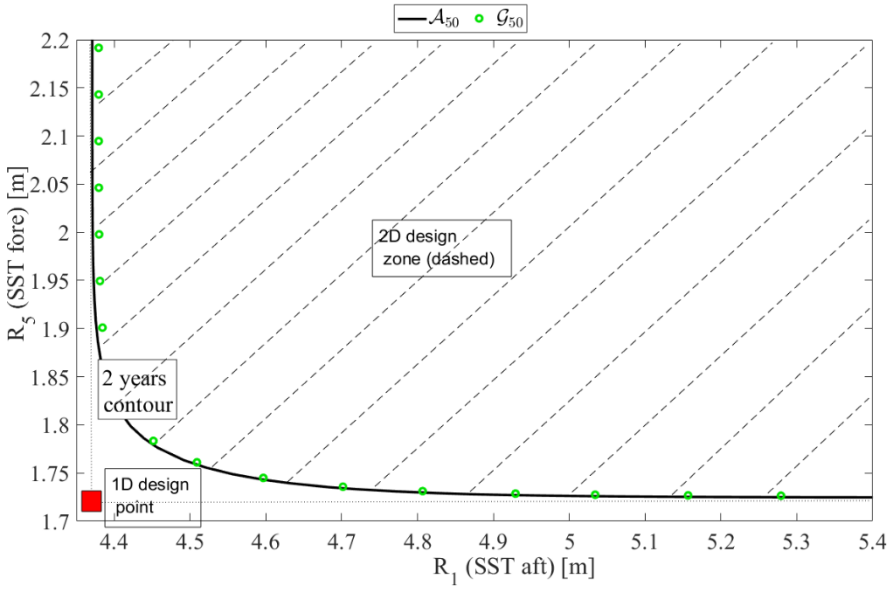

Figure 16 Design safe 2D zone (dashed) due to bivariate analysis, versus univariate 1D design point, based on Figure 15. Asymmetric logistic $\mathcal{A}_k(R_1, R_5)$ 2-years contour line.

Table 3 presents 5-year return period response predictions in meters, compared between the ACER and Gumbel methods. It is seen from the 95 % CI width that the ACER method offers more accurate predictions than the Gumbel fit.

Table 3 5-year return period response predictions in meters with 95 % CI in brackets.

	0.5 m/s	**1 m/s**
ACER R_1 (SST aft) 95 % CI	4.65 (4.21,5.29)	9.14 (7.70, 10.03)
Gumbel R_1 (SST fore) 95 % CI	5.12 (3.86, 6.01)	9.91 (7.24, 11.31)
ACER R_5 (SST fore) 95 % CI	1.77 (1.64, 1.91)	6.97 (5.54, 8.35)
Gumbel R_5 (SST fore) 95 % CI	1.79 (1.52, 2.05)	6.29 (4.76, 9.43)

6. Conclusions

The SST is an innovative subsea cargo drone in its very early stages of development with many research and development problems to be solved. Hydrostatic loading is a dominating load and drives the collapse design of the SST pressure hulls. This paper proposed using the ACER2D method to investigate the extreme positional responses (extreme surge and heave) during SST offloading in ocean current, considering that the aft thruster fails. Knowing the extreme positional responses is important because it gives the maximum depth, which determines the extreme hydrostatic load the SST will experience during operation. Further, the extreme surge motion will determine the length of the flowline required to avoid it being taut and resulting in snap loadings. The ACER2D method is implemented by expressing the long-term extreme value distribution in terms of the bivariate average conditional exceedance rate functions.

It is shown that the extreme responses with return periods of 5 years are, in general, higher than the maxima of the 4-hour response by a factor of two. This indicates that the thrusters could be required to be sized for two times the mean ocean current velocity speed. Further, it is seen that the response at the aft where the thruster fails is two times larger than the response at the fore of the SST.

Regarding the safety and reliability of vessel operation, the multivariate analysis is a more proper approach than the classic univariate approach. The presented bivariate technique has the following advantages:

- ACER2D method is Monte Carlo based and does not simplify inherent model non-linearities.
- Various kinds of coupled data can be studied: experimentally measured or numerically simulated.
- Clustering and narrow-band effects can be accounted for.
- Unlike various methods based on asymptotic assumptions, e.g., univariate Gumbel (which is also investigated in this paper), Pareto, POT, Weibull, the bivariate ACER2D method provides an accurate estimate of the exact bivariate extreme value without directly involving asymptotic assumptions.
- The ACER2D method may provide an efficient way of identifying bivariate copula models appropriate for practical design.
- A novel and more safe design approach has been outlined based on bivariate analysis.

The proposed approach in this paper is useful for further developing the SST design, assisting dynamic parameters optimization and minimizing potential vessel damage. Bivariate contours facilitate the choice of bivariate design points. This contrasts with using a pair of uncoupled univariate design points with the same return period, which is the current practice adopted in the industry. The univariate design approach has been shown to result in a non-conservative design factor. The multivariate analysis could lead to a safer vessel design extension of the bivariate approach. Lastly, the proposed method can be applied to other innovative subsea drones, such as the subsea freight-glider [36][37].

References

[1] Equinor Energy AS. 2019. RD662093 Subsea shuttle system.

[2] Ellingsen, K.E.; Ravndal O.; Reinas, R.; Hansen, J.H.; Marra, F.; Myhre, E.; Dupuy, P.M.; Sveberg, K. 2020. RD677082 Subsea shuttle system.

[3] Xing, Y.; Ong, M.C.; Hemmingsen, T.; Ellingsen, K.E.; Reinas, L. 2021. Design considerations of a subsea shuttle tanker system for liquid carbon dioxide transportation. Journal of Offshore Mechanical Arctic Engineering, 143(4), 045001.

[4] Ma, Y.; Xing, Y.; Ong, M.C.; Hemmingsen, T. 2021. Baseline design of a subsea shuttle tanker system for liquid carbon dioxide transportation. Journal of Ocean Engineering 240, 109891.

[5] Norwegian Petroleum Directorate (NPD). 2021. Carbon Capture and Storage. Available online: http://www.norskpetroleum.no/en/environment-and-technology/carbon-capture-and-storage/ (accessed on 1 August 2021).

[6] Xing, Y.; Santoso, T.A.D; Ma, Y. 2021. Technical – economic feasibility analysis of Subsea Shuttle Tanker, under review in Journal of Marine Science and Engineering.

[7] DNV-GL. 2018. Rules for Classification, Naval Vessels, Part 4 Sub-surface Ships (Chapter 1) Submarines.

[8] Jamissen, P.L.; Ma, Y.; Xing, Y.H. 2022. Probabilistic design of ring-stiffened cylindrical hull structures applied on large cargo submarines, under review in International Conference on Ocean, Offshore and Artic Engineering.

[9] Ma, Y.; Silva, M.S.D; Xing, Y.H.; Sui, D. 2022. Modelling of a subsea shuttle tanker hovering in ocean current, under review in International Conference on Ocean, Offshore and Artic Engineering.

[10] Ma, Y.; Sui, D.; Xing, Y.; Ong, M.C.; Hemmingsen, T.H. 2021. Depth control modelling and analysis of a subsea shuttle tanker. International Conference on Offshore Mechanics and Arctic Engineering, OMAE2021-61924, Virtual, Online, 21 – 30 June 2021.

[11] Luenberger, D.G. 1971. An Introduction to Observers. IEEE Transactions on Automatic Control, 16(6), 596-602.

[12] Prestero, T.T.J. 2001. Verification of a six-degree of freedom simulation model for the REMUS autonomous underwater vehicle (Master's thesis). Massachusetts Institute of Technology.

[13] Hoerner, S.F. 1965. Fluid-dynamic drag: Practical Information on aerodynamic drag and hydrodynamic resistance, Published by the author, California, USA.

[14] Blevins, R.D. 1979. Formulas for Natural Frequency and Mode Shape. Van Nostrand Reinhold Co. New York.

[15] Newman, J.N. 2017. Marine Hydrodynamics. MIT Press. Massachusetts.

[16] Barnitsas, M.M.; Ray, D.; Kinley, P. 1981. KT, KQ and efficiency curves for the Wageningen B-series propellers, University of Michigan.

[17] Drela, M. 1989. XFOIL: An analysis and design system for low Reynolds number airfoils, in Low Reynolds number aerodynamics, Springer, 1-12.

[18] Bowers, A.H.; Murillo, O.J.; Jensen, R.R.; Eslinger, B.; Gelzer, C. 2016. On wings of the minimum induced drag: Spanload implications for aircraft and birds. Technical report NASA/TP-2016-219072, NASA.

[19] Fossen, T. I. 2011 Handbook of marine craft hydrodynamics and motion control Wiley, Chichester, West Sussex.

[20] Sørensen, A.J. 2018. Marine Cybernetics (Lecture Notes). Norwegian University of Science and Technology. Trondheim.
[21] Ersdal G. 2001. An overview of ocean currents with emphasis on currents on the Norwegian continental shelf, Technical report, Norwegian Petroleum Directorate.
[22] Burlacu, P.; Dobref, V.; Badara, N.; Tarabuta, O. 2007. A LQR controller for an AUV depth control", Annals of DAAAM & Proceedings.
[23] Webb, D.C.; Simonetti, P.J.; Jones, C.P. 2001. SLOCUM: an underwater glider propelled by environmental energy, IEEE Journal of Oceanic Engineering 26(4), 447-452.
[24] Naess, A.; Moan, T. 2013. Stochastic dynamics of marine structures. Cambridge University Press.
[25] Naess, A.; Gaidai, O.; Batsevych, A. 2010. Prediction of extreme response statistics of narrow-band random vibrations, Journal of Engineering Mechanics, 136(3), 290-298.
[26] Naess, A.; Stansberg, C.; Gaidai, O.; Baarholm, R. 2009. Statistics of extreme events in airgap measurements, Journal of Offshore Mechanics and Arctic Engineering, 131(4), 041107.
[27] Naess, A.; Gaidai, O. 2009. Estimation of extreme values from sampled time series, Structural Safety, 31(4), 325-334.
[28] Naess A.; Gaidai O. 2008. Monte Carlo methods for estimating the extreme response of dynamical systems, Journal of Engineering Mechanics, 134(8), 628-636.
[29] Gaidai, O.; Xu, X.; Naess, A.; Cheng, Y.; Ye, R.; Wang J. 2020. Bivariate statistics of wind farm support vessel motions while docking, Ships and offshore structures, 16(2), 135-143.
[30] Gaidai, O.; Xu, X.; Wang J.; Cheng, Y.; Ye, R.; Karpa, O. 2020. SEM-REV offshore energy site wind-wave bivariate statistics, Renewable Energy, 156 , 689-695.
[31] Gao, H.; Gaidai, O.; Naess, A.; Storhaug, G.; Xu, X. 2018. Improving container ship panel stress prediction, based on another highly correlated panel stress measurement, Marine Structures, 64, 138-145.
[32] Gaidai, O.; Naess, A.; Xu, X.; Cheng, Y. 2019. Improving extreme wind speed prediction based on a short data sample, using a highly correlated long data, Journal of Wind Engineering & Industrial Aerodynamics, 188, 102-109.
[33] Gaidai, O., Naess, A., Karpa, O. Cheng, Y., Ye, R., (2019), "Improving extreme wind speed prediction for North Sea offshore oil and gasfields", https://doi.org/10.1016/j.apor.2019.04.024.
[34] Xu, X.; Gaidai, O.; Naess, A.; Sahoo, P. 2019. Improving the prediction of extreme FPSO hawser tension, using another highly correlated hawser tension with a longer time record, Applied Ocean Research, 88, 89–98.
[35] Naess, A.; Karpa, O. 2015. Statistics of extreme wind speeds and wave heights by the bivariate ACER2D method, Journal of Offshore Mechanics and Arctic Engineering, 137(2), 21602.
[36] Xing, Y. A conceptual large autonomous subsea freight-glider for liquid CO2 transportation. International Conference on Offshore Mechanics and Arctic Engineering, OMAE2021-61924, Virtual, Online, 21 – 30 June 2021.
[37] Ahmad, U.N.; Xing, Y. 2021. A 2D model for the study of equilibrium glide paths of UiS Subsea Freight-Glider, IOP Conference Series. Materials Science and Engineering, 1201(1), 012022.